



Comprehensive Analysis of the Aging Behavior of Nickel-Rich, Silicon-Graphite Lithium-Ion Cells Subject to Varying Temperature and Charging Profiles

Markus Schindler,^z  Johannes Sturm,^{id}  Sebastian Ludwig,^{id}  Axel Durdel,^{id}  and Andreas Jossen 

Institute for Electrical Energy Storage Technology (EES), Technical University of Munich, 80333 Munich, Germany

Especially for material combinations incorporating silicon-graphite anodes and nickel-rich cathodes, lifetime and energy density have to be balanced appropriately. In particular, silicon-graphite anodes show increased aging effects due to the extensive volume expansion of silicon and even small variations of its content lead to significant changes in the cell properties because of its large specific capacity. Two batches of the same cell, which differ slightly in their silicon content, were investigated using various charging profiles for a temperature range from 0 °C to 40 °C. The total number of EFC of both cell batches was shown to be strongly dependent on temperature. In addition, cells with reduced silicon content showed EFCs three times higher than their higher silicon counterparts. Contrary to expectations, an extended CV-charging sequence led to an increase in EFC and a decrease in variance. The exclusion of critical voltage ranges shows the most significant influence on both the total of EFC and the variance between the cells. As a result, to increase cell lifetime it is recommended that cells should be preconditioned at low ambient temperatures and extended CV-charging sequences should be considered. If the operational strategy allows the reduction of the upper-voltage-limit, critical voltage areas should be avoided.

© 2021 The Author(s). Published on behalf of The Electrochemical Society by IOP Publishing Limited. This is an open access article distributed under the terms of the Creative Commons Attribution 4.0 License (CC BY, <http://creativecommons.org/licenses/by/4.0/>), which permits unrestricted reuse of the work in any medium, provided the original work is properly cited. [DOI: 10.1149/1945-7111/ac03f6]



Manuscript submitted February 7, 2021; revised manuscript received April 26, 2021. Published June 28, 2021.

Energy storage systems in the fields of power tools, stationary energy storage systems, or transportation systems continuously demand higher storage capacities of their integrated lithium-ion batteries (LIBs).^{1–3} The capacity of a single LIB is determined by the capacities of the anode, the cathode, and the balancing between them. In regard to the cathode, nickel-rich materials offer a promising possibility to increase the capacity.^{4,5} To increase the energy density of the anode side past the commonly used 372 mAh g⁻¹ of pure graphite,^{6–8} it is common to add materials with greater energy densities.^{9–13}

Silicon offers a theoretical energy density of up to 3579 mAh g⁻¹ and therefore offers a theoretically huge increase in the capacity of the anode.^{4,6,8,14,15} In addition to the high energy density, it is easily accessible, environmentally friendly, and comes with low manufacturing costs.^{16,17} If a cell manufacturer produces LIB with novel material combinations, the goal is to achieve both a higher energy density than traditional material combinations as well as similar or improved aging behavior.

For established material combinations such as graphite on the anode side and lithium iron phosphate (LFP), lithium cobalt oxide (LCO), lithium nickel cobalt aluminum oxide (NCA), or lithium nickel manganese cobalt oxide (NMC) on the cathode side, numerous aging studies can be found in the literature.^{6,18–29} These describe in detail the causes and indications of aging mechanisms, and classify them into categories such as loss of lithium inventory (LLI), loss of active material (LAM) at the anode and cathode side or loss of electrolyte.³⁰ For novel material combinations, especially for silicon-graphite (SiC)/NMC-811, such investigations are currently only available to a limited extent in the literature.^{4,6,14,31,32} The LG INR18650MJ1 (MJ1) cell investigated in this work incorporates such a material combination and is named by Popp et al.³¹ as one of the state-of-the-art high energy cells available on the consumer market. For this reason its use is increasing both in industry and research.^{6,31–36} In SiC anodes, the challenge is to optimize the content of silicon to achieve the required energy density level, without triggering premature aging caused predominantly by the mechanical expansion of silicon (up to 300%).^{4,6,15,16,31} If the silicon content is too high, increased particle cracking, loss of particle contact, solid electrolyte interface (SEI) cracking and repair

processes, as well as lithium plating are possible consequences which in turn lead to rapid cell aging.^{8,16,37} On the other hand, nickel-rich NMC cathodes like NMC-811 are sensitive to parasitic reactions with the electrolyte, surface restructuring, oxygen release, cation mixing, active material dissolution, and particle cracking.¹⁴ Additionally, Jung et al.³⁸ showed that the cutoff voltage is a key parameter for cyclic stability of NMC cathodes.

Baumhöfer et al.¹⁸ emphasized the irreplaceability of aging experiments in quantifying the influence of such aging phenomena. Therefore, an overview of recently published aging experiments at the cell level using MJ1 cells is presented in Table I. Li et al.⁶ analyzed changes of morphology, crystal structure, electrochemical properties, and elemental composition and concluded that SEI growth on the anode side as well as loss of active material on both electrodes are the main degradation mechanisms. Lithium plating could not be detected within this study. Measurements were conducted at an ambient temperature of 25 °C. Constant current (CC) charge (I_{Ch-CC}) and discharge (I_{Dch-CC}) currents of 0.5 C were applied between 2.5 V and 4.2 V with constant voltage (CV) charging (I_{Ch-CV}) at 4.2 V to 50 mA. No measurements were taken at varying temperatures or charging profiles. Popp et al.³¹ compared eight high-energy cells, including LG's MJ1, and evaluated the cyclic aging performance for two different charging rates (0.5 C, 1 C). For all aging experiments, CC discharging (1 C) and CV charging/discharging (175 mA) were used. Capacity checkups were performed at three different temperatures (10 °C, 25 °C, 45 °C) with a view to automotive applicability. However, cell cycling was performed solely at 25 °C. For an average state of charge (SOC) of 50%, a depth of discharge (DOD) of 60% showed the lowest aging rates. Reduced upper voltage limits or varying CV charging limits would have been of particular interest here, but were not discussed. Accordingly, the influence of the charging profile was only analyzed to a small extent and the influence of different cycling temperatures were not addressed. In contrast to Li et al.,⁶ the exact causes of aging were only dealt with superficially within the work of Popp et al.³¹ Kok et al.³² used X-ray computed tomography to investigate differences in the jelly-roll over its lifetime and showed that for both electrodes, the region most sensitive to delamination and aging is the innermost region next to the current collector. Lastly, Heenan et al.¹⁴ analyzed aging mechanisms at the cell-, electrode-, and particle-level and clustered the intensity of aging into the categories:

^zE-mail: markus.ms.schindler@tum.de

Table I. Summary of recently published single cell aging experiments with MJ1 cells. In Ref. 32 only the temperature (T) was specified.

References	T in °C	$I_{\text{Ch-CC}}$ in A	$I_{\text{Ch-CV}}$ in mA	$I_{\text{Dch-CC}}$ in A	$I_{\text{Dch-CV}}$ in mA
6	25	0.5 C	50	0.5 C	—
31	25	0.5 C, 1 C	175	1 C	175
32	25	—	—	—	—
14	25	≈0.4 C	100	≈1.2 C	—

initial loss, beginning of life (BOL) loss, and long duration degradation. During cyclic aging, cells were charged at 1.5 A (≈0.4 C) and discharged at 4 A (≈1.2 C) between 2.5 V and 4.2 V. CV charging up to the cutoff current of 100 mA was applied at 4.2 V between charging and discharging. All measurements were carried out at an ambient temperature of 25 °C. Accordingly, the influences of temperature, different charging profiles, and the production batch on the aging behavior of the cell under investigation are currently not sufficiently discussed in literature.

In this work we present a comprehensive aging experiment, incorporating five different aging studies using 40 cells. Within these studies, the aging behavior of cells from two different production batches with varying silicon contents is investigated, since the batch can have a non-negligible effect on the cell properties.³⁵ The temperature behavior as well as different charging profiles are analyzed in detail to show the influences of CV charging and upper cell voltage limits. Before starting the aging experiment, initial cell-to-cell variations were minimized through cell matching to investigate the findings of Dubarry et al.,³⁹ who claimed that limited initial cell-to-cell variations of capacity and impedance result in a low variation of the cells' aging behavior. Furthermore, we analyze whether, if extended CV charging or reduced upper cell voltage limits lead to an increased cycle lifetime and a lower variance of the aging behavior of the investigated cells. For the detection of the state of health (SOH), a checkup routine is presented, which was utilized in prior publications.^{23,24,33,36} The increase of internal impedance R_i is monitored via electrochemical impedance spectroscopy (EIS). For more in-depth analysis of the aging mechanisms, differential voltage analysis (DVA) as well as microscope analysis of the jelly role and scanning electron microscope (SEM) analysis from harvested anode and cathode active materials are carried out. To the best of our knowledge, we firstly investigate the aging behavior of individual cells from different production batches containing a high energy SiC/NMC-811 cell chemistry.

Experimental

Cell under investigation.—We tested commercial 18650 lithium-ion cells from two different production batches, manufactured by LG Chem. The cells were produced in 09/2016 (B₁) and 10/2017 (B₂). The cells incorporate SiC active material on the anode side and nickel-rich NMC as a cathode material.^{14,34,36} The minimum reversible capacity of the cells is given as 3.35 Ah by the manufacturer. The measured mean capacities and energy densities of

B₁/B₂ calculate to 3.49 Ah/3.43 Ah and 274 Wh kg⁻¹/268 Wh kg⁻¹, respectively. As described within our previous work, the decreased mean capacity and energy density of B₂ are most likely caused by a slightly reduced silicon content within the anode.³⁶ Based on the DVA and differential capacity analysis (DCA) in our previous work Ref. 36 we would estimate that the silicon content has decreased slightly to approximately 3.2 wt% or 3.3 wt% for cells of B₂, as compared to the measured silicon content of around 3.5 wt% (ICP-OES³⁴) for cells of B₁.

Storage conditions.—To ensure equal starting conditions and to reduce side reactions as well as the influence of the anode overhang, cells were stored at 50% SOC and 5 °C after delivery and initial characterization. The time between storage after initial characterization and the start of the aging experiment was 140 days on average for cells from B₁ and 175 days for cells from B₂. This difference in storage times is not assumed to have significantly affected the aging rate.

Measurement equipment.—Cycling and capacity checkup routines were performed using a battery cyclers (CTS, BaSyTec). Checkup routines of the internal impedance were done via galvanostatic EIS measurements using a potentiostat (VMP3, Biologic). At the end of the experiment, cells were opened, unrolled and harvested inside an Argon-filled glove box (M. Braun Inertgas-Systeme). The microscope analyses (INSPEX II, Ash Vision) were also conducted inside the glove box. SEM measurements were carried out using a scanning electron microscope (JSM-IT200 InTouchScope, JEOL). Climate chambers were used to achieve constant ambient temperatures during cycling and checkup routines.

Aging experiment.—To obtain a detailed understanding of the influence of different production batches on the aging behavior, cells of B₁ and B₂ were cycled within study ① using identical cycling profiles (see Table II). The CC charging rate ($I_{\text{Ch-CC}}$) and the cutoff criterion for CV charging ($I_{\text{Ch-CV}}$) of study ① was selected with respect to the limits given by the cell manufacturer. The CC-discharge rate ($I_{\text{Dch-CC}}$) and the CV discharging cutoff criterion ($I_{\text{Dch-CV}}$) were accordingly based on $I_{\text{Ch-CC}}$ and $I_{\text{Ch-CV}}$. To investigate the influence of different charging profiles, studies ②-⑤ were applied to cells from B₂. Study ② can be seen as the reference aging study for B₂. In contrast to study ①, the charging current is reduced from the maximum charging current (1 C) to the nominal charging current (0.5 C). Additionally, the CV charging cutoff criterion is increased from 33.5 mA to 100 mA. These changes have been made to counteract the accelerated aging behavior of profile ① (see Figs. 3a and 3b) and to achieve shorter CV cutoff criteria, which is more representative of real-world applications.³¹ The CV discharge was omitted due to its low practical relevance.⁴⁰ In study ③, the influence of a longer CV charging as compared to study ② is investigated. Finally, in studies ④ and ⑤ the impact of the charging cutoff voltage on the aging behavior is analyzed.

The cutoff voltages of 4.089 V and 4.115 V were determined with reference to the DCA (see Fig. 1) applied to the cells of this work. The global maximum I at 4.072 V of the DCA arises from a voltage plateau in the measured open-circuit-voltage (OCV).

Table II. Summary of parameters for each of the five studies. Study ① investigates cells of B₁ and B₂, studies ② to ⑤ only cells of B₂. Cells were cycled at 0 °C, 10 °C, 25 °C, or 40 °C in studies ① and ②. Within study ①, no cells were cycled at 40 °C due to limited resources. Studies ③ to ⑤ were performed at an ambient temperature of 25 °C. t_{pause} describes the pause for thermal relaxation between the charging and the discharging sequence.

Study	Batch	$I_{\text{Ch-CC}}$ in A	$I_{\text{Ch-CV}}$ in mA	$I_{\text{Dch-CC}}$ in A	$I_{\text{Dch-CV}}$ in mA	U_{min} in V	U_{max} in V	t_{pause} in h
①	B ₁ , B ₂	1 C	33.5	1 C	33.5	2.5	4.2	0.5
②	B ₂	0.5 C	100	1 C	—	2.5	4.2	0.5
③	B ₂	0.5 C	33.5	1 C	—	2.5	4.2	0.5
④	B ₂	0.5 C	100	1 C	—	2.5	4.089	0.5
⑤	B ₂	0.5 C	100	1 C	—	2.5	4.115	0.5

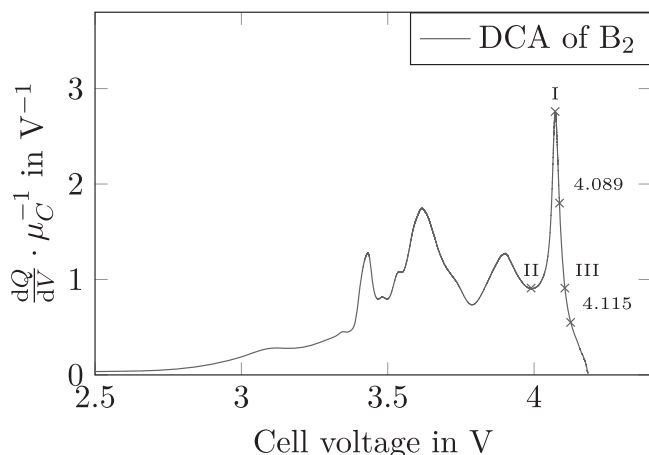


Figure 1. The DCA curve of B₂ displayed here represents the averaged DCA of all single cell DCAs (see³⁶). The corresponding voltage values of 4.089 V and 4.115 V are used to investigate the influence of the upper voltage limit on the aging behavior. μ_C represents the mean capacity of all cells of B₂, calculated in Ref. 36. Mark I corresponds to the global maximum of the DCA, mark II to the local minimum on its left, and mark III represents DCA equal to mark II, but on the right side of the global maximum.

Because of the plateau, even slight changes in voltage have a large effect on the SOC, which is why it is difficult to use the corresponding voltage level as a defined upper voltage limit. The at least exponential decrease in capacity gain to the right of the global maximum I does not suffer from this problem and forms the basis of the determination of the upper cell voltage limit in the ④ and ⑤ studies. The value of 4.089 V was then determined as follows: On the right side of the global maximum I, a DCA level equal to the local minimum II was marked. This is represented by III and corresponds to 4.106 V. The voltage level of 4.089 V therefore corresponds to the mean voltage difference between 4.072 V (I) and 4.106 V (III). For the second point, it is noted that the gradient of the DCA curve changes slightly after 4.115 V. A voltage value was chosen that was situated between point III and this change of gradient. The exact value was then determined by adding half of the voltage difference between III and 4.089 V to the voltage value of III (4.106 V). The restriction of the maximum charging voltages to 4.089 V and 4.115 V corresponds to a reduction of the usable SOC window to 97.36% and 97.98%, respectively.

The influence of varying ambient temperatures during cyclic aging is analyzed through studies ① and ②. Profiles ① (only for B₁) and ② were applied at an ambient temperature of 0 °C, 10 °C, 25 °C, or 40 °C. Cells of B₂ were only aged at ambient temperatures of 0 °C, 10 °C, and 25 °C within study ① due to limited resources. All other studies were performed at an ambient temperature of 25 °C. To reduce the influence of cell heating during charging/discharging on

the subsequent discharging/charging sequence, a pause (t_{pause}) for thermal relaxation of 0.5 h^{41,42} was introduced between successive charging or discharging sequences. Table II summarizes the parameters used in each of the five studies.

To ensure statistical significance, three cells were measured at each measuring point. Prior to the aging studies, a sorting process was applied for cells of B₂ to ensure similar initial capacity (measured using a constant current-constant voltage (CC-CV) protocol) and R_i ($\text{Im}(Z) = 0$) of the cells at the beginning of the experiment. The sorting strategy prioritized equal capacities over equal internal impedances. The measurement and evaluation procedures to obtain the values for capacity and internal impedance are described in detail in our previous work.³⁶ Table A-1 provides an overview of initial capacity and internal impedance matching for all studies using cells of B₂ within the experiment.

Checkup routines.—The development of the SOH, R_i , and the OCV was recorded by regular checkup routines at an ambient temperature of 25 °C. To minimize the influence of different cycling temperatures, cells were acclimatised at 25 °C prior to the checkup routine. The resting time for thermal relaxation was selected in relation to the cycling temperature. Cells cycled at an ambient temperature of 0 °C or 40 °C were acclimatised for 5 h before starting the checkup routine. Cells cycled at 10 °C were acclimatised for 3 h. For cells cycled at 25 °C, a resting time of 1 h was established between cycling and checkup routines to diminish any influence of cell heating during cycling. Pretests verified that the chosen times were sufficient for thermal homogenization. Figure 2 gives an overview of the sequences of events.

Capacity measurements to determine the SOH were performed using the profile described in Table III. The cell voltage limits were set to 4.2 V and 2.5 V, as recommended by the manufacturer. The applied charge $I_{\text{Ch-CC}}$ and discharge $I_{\text{Dch-CC}}$ currents as well as the cutoff current of 50 mA during CV charging $I_{\text{Ch-CV}}$ were chosen according to the manufacturer's data sheet. The cutoff criteria during CV discharging $I_{\text{Dch-CV}}$ was based on $I_{\text{Ch-CV}}$. Subsequently, the parameter R_i was determined at a SOC of 50% using galvanostatic EIS. The measurement was performed within the frequency range of 10 mHz to 10 kHz, with a current amplitude of 140 mA. Finally, R_i was evaluated at $\text{Im}(Z) = 0$. This measurement procedure has been used by^{23,33} and is also used in the initial cell characterization of this study.

At the beginning of the experiment, checkup routines were therefore undertaken every seven cycles to track the aging behavior as accurately as possible. These checkups comprised capacity and EIS measurements. An OCV measurement was done only every 14 cycles due to the comparatively long measuring time of approximately 85 h. Since accelerated aging behavior was expected for studies at 0 °C, an OCV measurement was also recorded every seven cycles. In general, OCV measurement was done during a single charge-discharge cycle (CC-CV) at a small current of 0.03 C. As our understanding of the aging behavior shown within the different studies improved, the checkup interval was gradually increased. The

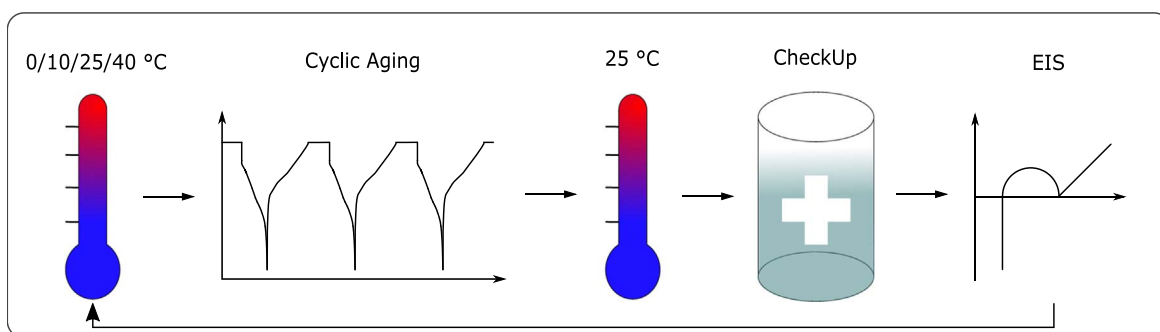


Figure 2. Sequences of events in the aging experiment. Cells were stored at the respective study temperature prior to cyclic aging and at 25 °C before checkup routines. Checkup routines were used to determine cell capacity and internal impedance progression.

Table III. Overview of regular checkup routines. Cell capacity was determined by the sum of CC and CV discharge capacity. R_i was determined by an EIS at 50% SOC ($\text{Im}(Z) = 0$). Cells were cycled between 4.2 V and 2.5 V. $I_{\text{Ch-CV}}$ and $I_{\text{Dch-CV}}$ represent the absolute cell current limits of the corresponding CV phase. OCV measurement was done during a single charge-discharge cycle (CC-CV) with small current. t_{pause} describes the pause for thermal relaxation between the charging and the discharging sequence. All tests were performed at an ambient temperature of 25 °C.

Sequence	$I_{\text{Ch-CC}}$ in A	$I_{\text{Ch-CV}}$ in mA	$I_{\text{Dch-CC}}$ in A	$I_{\text{Dch-CV}}$ in mA	t_{pause} in h
Capacity Check	0.5 C	50	0.2 C	50	0.5
EIS ^{a)}	—	—	—	—	—
OCV	0.03 C	3.5	0.03 C	3.5	6

a) f in [10 mHz; 10 kHz], $\hat{I} = 140$ mA, 13/10/5 points per decade within [10 kHz; 1 Hz]/[1 Hz; 100 mHz]/[100 mHz; 10 mHz].

first increase was from seven to 21 cycles. Later on, this interval was increased further to 42 or 56 cycles.

Limitations.—Due to limited resources, not all experiments could be performed with the same number of cells per study or at all investigated temperatures. Therefore, cells from B₂ are excluded from cycling at 40 °C within study ① and within studies ④ and ⑤ only two cells were cycled per study.

Results

This section describes the results of the studies introduced in Table II.

Study ①.—Figure 3 illustrates the evolution of the SOH for B₁ (a) and B₂ (b), both cycled within study ①. As described earlier, no cells of B₂ were aged at 40 °C. Comparing the number of equivalent full cycles for cells of B₁ for different temperatures, cells cycled at 0 °C, 10 °C, 25 °C, and 40 °C reached a respective maximum of 18, 76, 86, and 196 EFC before a SOH level of 80% was reached. Cells of B₂ reached 76, 113, and 336 EFC for 0 °C, 10 °C, and 25 °C, respectively. This corresponds to Factors_{B₁→B₂} of 4.2, 1.5, and 3.9 between the maximum number of EFC reached for cells of B₁ and B₂ at 80% SOH and equal temperatures. All cells in study ① cycled at 0 °C and 10 °C displayed non-linear aging. The same is true for cells of B₁ cycled at 25 °C. Cells of B₂ cycled at this temperature, showed a different trend since the slope changed after 14 EFC and a more linear aging was observed until the end of life (EOL). The cycling of B₁ at 40 °C showed both, linear aging to 150 EFC and non-linear aging afterwards.

Figure 3 also illustrates the respective evolution of R_i for cells of B₁ (c) and B₂ (d). Regardless of temperature, cells from B₁ show a nonlinear increase in R_i at the EOL, although the 25 °C and 40 °C cells undergo a transition from linear to non-linear growth only shortly before this point. The percentage increase of R_i at the EOL of cells with the highest number of EFC are: 160% (0 °C), 132% (10 °C), 112% (25 °C), and 124% (40 °C). The R_i of the cells from B₂ are seen to decrease initially, before increasing monotonically. The rate of increase shown by the 0 °C and 10 °C measurements appear very similar. The increase in R_i of cells cycled at 25 °C is less pronounced as compared to the other temperatures. At EOL, cells' R_i has increased by 118% (0 °C), 114% (10 °C), and 117% (25 °C). Subtraction of the percentage increase in R_i in B₁ at a SOH of 80% from its equivalent in B₂ allows the increases to be compared. Thus B₂ displays resistances 42% and 18% lower than those from B₁

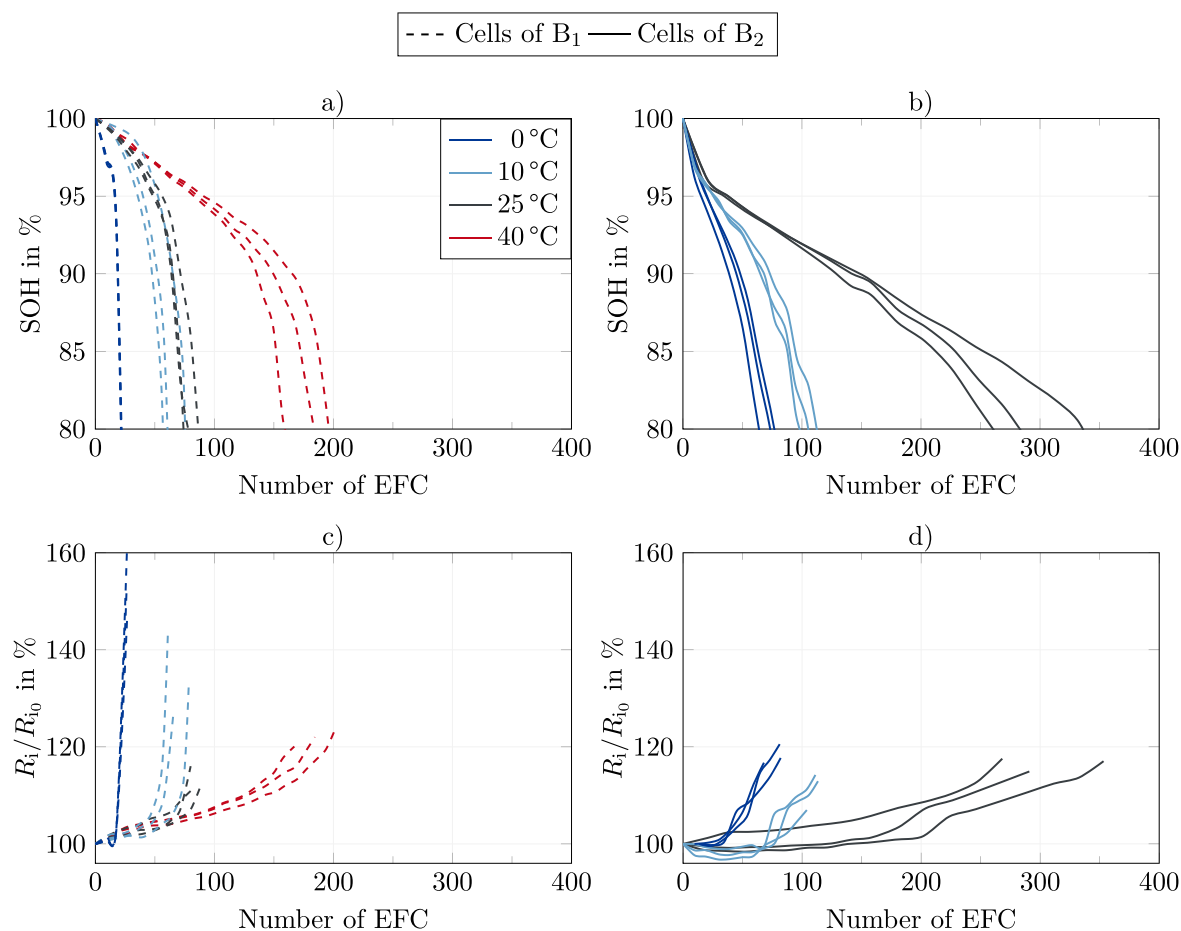


Figure 3. Evolution of SOH (a), (c) and R_i (b), (d) for cells of B₁ (dashed) and B₂ (solid) cycled within study ①. The line colors indicate the temperature during cyclic aging.

Table IV. Summary of EFC and R_i differences between B_1 and B_2 , cycled within study ① at 80% SOH. $\text{Factor}_{B_1 \rightarrow B_2}$ describes the number of EFC reached by the cells of B_2 as a multiple of those achieved by B_1 at the given temperatures. $\Delta R_{i, B_1 \rightarrow B_2}$ describes the difference of the respective R_i increases in % of B_2 to B_1 .

T in °C	EFC _{B₁} in—	EFC _{B₂} in—	Factor _{B₁→B₂} EFC _{B₂} /EFC _{B₁}	R_{i, B_1} in %	R_{i, B_2} in %	$\Delta R_{i, B_1 \rightarrow B_2}$ in %
0	18	76	4.2	160	118	−42
10	76	113	1.5	132	114	−18
25	86	336	3.9	112	117	5
40	196	—	—	124	—	—

Table V. Summary of EFC reached at 80% SOH within study ②. Taking the number of EFC reached at 25 °C as a reference, $\Delta \text{EFC}_{T \rightarrow 25^\circ\text{C}}$ describes the percentage of EFC reached for the respective temperature.

T in °C	EFC in—	$\Delta \text{EFC}_{T \rightarrow 25^\circ\text{C}}$ in %
0	150	23
10	320	50
25	645	100
40	560	87

Table VI. Cell-to-cell variations between the maximum and minimum EFC achieved for each temperature at 80% SOH. Within study ③, the second cell only decreased to 83% SOH. Cells of studies ④ and ⑤ only decreased to 86%/85% and 85%/83% SOH. All values in %.

Study	Batch	0 °C	10 °C	25 °C	40 °C
①	B ₁	0.0	33	18	24
①	B ₂	21	15	29	—
②	B ₂	15	19	20	7.7
③	B ₂	—	—	0.7	—
④	B ₂	—	—	0.4	—
⑤	B ₂	—	—	0.9	—

when cycling at 0 °C and 10 °C. The resistance increase after cycling at 25 °C was 5% greater in B_2 than in B_1 . Table IV summarizes these values.

Study ②.—Figure 4 illustrates the temperature dependency of SOH (a) and R_i (b) for cells cycled within study ②. As the cycling temperature increases from 0 °C to 25 °C, the cyclic stability also increases. Due to the steep gradient of the 0 °C curves, non-linear aging is assumed for these cells. The maximum number of EFC reached amounts to 150 for cells cycled at 0 °C. The SOH progression of cells cycled at 10 °C appears flatter as compared to those cycled at 0 °C, especially in the range between 50 and 200 EFC. The corresponding maximum number of EFC at 80% SOH at 10 °C reaches to 320. Cells cycled at an ambient temperature of 40 °C show similar performance to cells cycled at 25 °C. However, the increased loss of SOH around 180 EFC leads to a smaller number of EFC at the EOL as compared to cells cycled at 25 °C. The maximum numbers of EFCs at 25 °C and 40 °C totaled 645 and 560 respectively.

Taking 25 °C as the reference temperature, cells cycled at 0 °C, 10 °C, and 40 °C only reached 23%, 50%, and 87% of the EFC of the cells at the reference temperature. Table V summarizes these values. Comparing the respective number of EFC for cells cycled at

the same ambient temperature at 80% SOH, variations of 15%, 19%, 20%, and 7.7% were present between the cells measured at 0 °C, 10 °C, 25 °C, and 40 °C. Table VI summarizes the variations between the cells with the lowest and highest number of EFC for the investigated temperatures and studies. The respective progressions of cell impedances R_i are shown in Fig. 4b. Similar to the results illustrated in Fig. 3d, the R_i decreases initially and is then followed by a linear or non-linear increase. After the initial decrease, R_i of cells cycled at 0 °C shows an immediate non-linear increase, whereas cells at 10 °C first display a linear increase, which after approximately 200 EFC then leads into a non-linear progression. The R_i of cells cycled at ambient temperatures of 25 °C and 40 °C increases linearly. The topmost line representing one of the 40 °C cells is deemed to be an outlier, since it shows an anomaly between 190 and 220 EFC, after which the gradient returns to that of the other cells at the same temperature. The final change in recorded impedance R_i for cells with the highest number of EFC amount to 104.5% (0 °C), 106.5% (10 °C), 107.4% (25 °C), and 114% (40 °C). Variations between the final resistance values measured in cells cycled at a given temperature remain below 1% for 0 °C, 10 °C, and 25 °C. The final resistance values for the cells measured at 40 °C

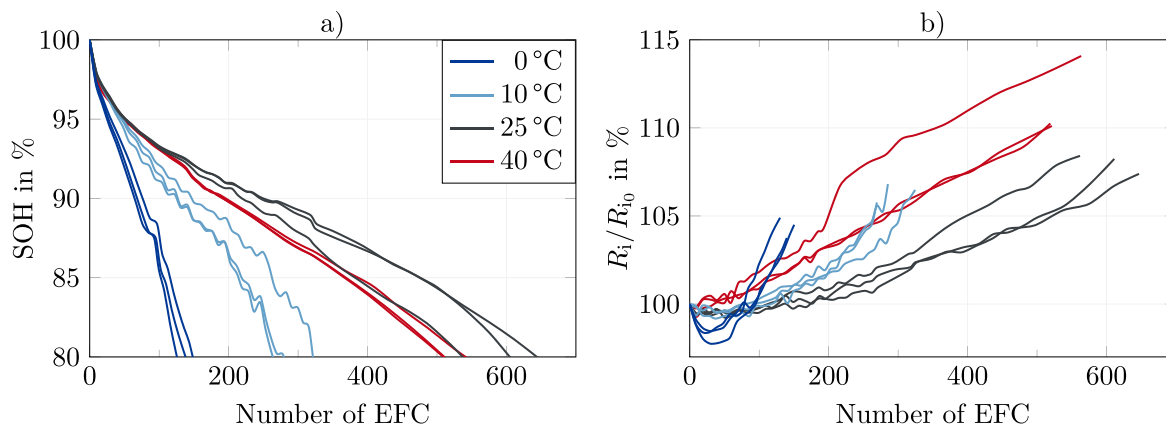


Figure 4. Evolution of SOH (a) and R_i (b) for cells cycled within study ②. The line colors indicate the temperature during cyclic aging.

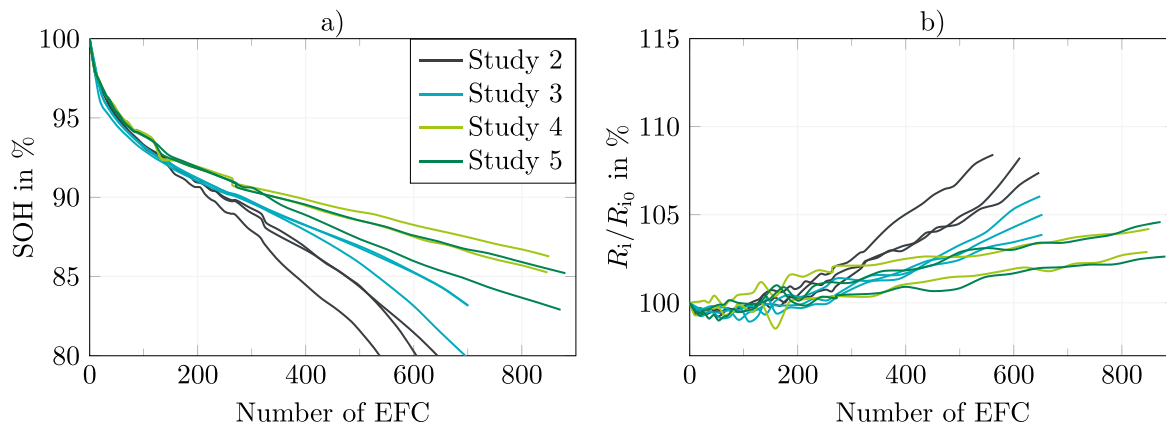


Figure 5. Evolution of SOH (a) and R_i (b) for studies ② to ⑤. Note that only results for 25 °C are illustrated for study ② since studies ③ to ⑤ only were taken at ambient temperatures of 25 °C.

vary by 4% due to the increased gradient seen in one of the cells between 190 and 220 EFC.

Studies ③ to ⑤.—The evolution of SOH and R_i of studies ③ to ⑤ are illustrated in Fig. 5. To better compare the progression to the reference study ②, the latter is also shown for 25 °C. For studies ③ to ⑤, only one cell from study ③ reached 80% SOH (695 EFC) during the aging study. The remaining cells of study ③ ended with a SOH of 83% and 700 EFC. Cells from study ④ ended with SOHs of 86% and 85%. The corresponding EFCs amount to 850 and 847. The final EFCs from study ⑤ were 880 and 872 with corresponding SOHs of 85% and 83%. Table VI also summarizes the variations for studies ③ to ⑤.

Taking the final number of EFC from the cell with the highest aging rate at a given temperature as a reference, the differences in the SOH between the cells at that temperature can be compared. For the reference study ②, a difference of 7% SOH between the cells can be seen at a SOH of 80%. At the same SOH, the difference amounts to 3% between the cells of study ③. For studies ④ and ⑤, respective differences of 1% and 3.3% are seen at the final SOHs of 85% and 83%. The analysis of R_i development illustrated in Fig. 5b shows linearly increasing values for all cells cycled within studies ③ to ⑤. Cells of the reference study ② show the steepest slope, cells of studies ④ and ⑤ the lowest gradients. At the beginning, R_i of studies ② and ③ are within the same range, but from approximately 300 cycles on, cells of study ② markedly exceed those of study ③. The final resistance R_i of the different studies in Fig. 5b at the respective maximum EFC amounts to 108.4%, 106%, 104.6%, and 104.2% for studies ② to ⑤.

Discussion

If one compares the aging characteristics of the different batches within study ①, significantly higher numbers of EFC are demonstrated by the cells of B₂ vs those of B₁. This is the case for every temperature profile included in the study. Since the storage time after initial characterization and the start of the respective experiment for cells of B₁ and B₂ was within the same range and the cycling profile was identical, it is likely that varying material compositions of the batches are accountable for the different aging behaviors. The decreased capacity of B₂ as compared to that of B₁ is discussed within our previous work³⁶ and additionally, DVA showed that the smaller capacity is most likely caused by a slightly reduced silicon content within the anode, rather than by adapted electrode balancing. It is therefore also assumed that the higher numbers of EFC reached by B₂ are related to the decreased silicon content within the anode. Lory et al.¹⁶ related that the silicon particles are embedded within a carbon matrix which is responsible for the transport of lithium during lithiation/delithiation and also buffers the expansion of the

silicon particles. Assuming that B₁ and B₂ show almost identical porosities, a higher silicon content in B₁ may be associated with a lower graphite content. Therefore, fewer carbon matrix structures are available to embed the silicon particles. Consequently, the reduced graphite content would lead to a less effective buffering of the silicon expansion^{8,16} and as such, degradation mechanisms like particle cracking, loss of contact between particles and current collector, as well as SEI crack and repair processes are assumed to increase accordingly. These forced degradations of the electrode material would result in a more rapid loss of capacity as well as an increased R_i growth, both of which are shown in Fig. 3. Consequently, the aging behavior of the cells differs significantly between both batches. It is conceivable that alterations by the manufacturer to the electrolyte and/or additives in the cell may have affected the aging behavior of the cell. This hypothesis could not be tested in this study due to the methods employed.

Furthermore, in this work, charge and discharge parameters of study ① place the greatest demands on the cell. CC-CV discharging leads to a deeper delithiation of both, graphite and silicon particles within the anode and causes increased particle swelling during discharge and the following charging sequence as compared to pure CC discharging. Future studies should therefore analyze the influence of the CV discharge sequence by isolated variation of this parameter. Additionally, in study ①, the charging current of 1C forces a higher potential gradient between the solid and the liquid interface as compared to the charging current of 0.5 C in studies ② to ⑤.^{16,43} Especially toward the end of CC charging, the increased polarization within the anode can lead to an anode voltage level which may result in lithium plating.^{43,42} Considering the non-linearity of the aging curves of study ① (see Fig. 3), it seems very likely that, in addition to the effects of silicon expansion, lithium plating was also an influencing factor.²⁴ To support these statements, Fig. 7a shows the change in DVA for a representative cell of B₁ cycled at 0 °C at 80% SOH as compared to the reference cell of B₁ at 100% SOH. For the pristine cell, the anode and cathode markers are clearly distinguishable. The markers are categorized to silicon, graphite, and NMC markers and named S_I and S_{II}, C_I, C_{II}, C_{III}, and C_{IV}, as well as NMC_I and NMC_{II}, respectively.^{33,36,42} A change in the storage capacity of the different active materials can be detected in the DVA by altering distances between the markers. Therefore, decreasing distances between S_I and S_{II}, NMC_I and NMC_{II}, or C_I (main graphite peak) and the right border of the DVA indicate a decrease of the storage capacity of the respective active material.^{23,42} Compared to the reference DVA at 100% SOH, the DVA at 80% SOH displays a strong decrease of the anode capacity for cells cycled at an ambient temperature of 0 °C. This can be seen from the decreased distance between S_I and S_{II}, whereby one of the silicon markers is no longer present in the DVA spectrum. Furthermore, the broadening of the main graphite peak C_I at around 1.4 Ah (100%

(SOH), the no longer detectable markers C_{II} , C_{III} , and C_{IV} , as well as the shortened distance from the main graphite peak C_I to the maximum extractable capacity (right border) show the degradation of the anodes capacity. According to Keil,⁴⁴ in particular the broadening of the elevated main graphite peak can be attributed to inhomogeneous degradation of the anode active material. These findings are further supported by the microscope analysis and the SEM measurements shown in Figs. 8a and 8c, where the delamination of anode active material can be clearly detected. Additionally, the SEM measurement in Fig. 8a shows a fracture edge of the anode material extracted from the inner area of the jelly roll. On the surface of the uppermost particles, surface layers can be depicted (Fig. 8a, I), whereas particles in underlying areas seem to be not or only slightly affected (Fig. 8a, II), which reveals the inhomogeneous degradation of the active material particles. An exact composition of the surface layer cannot be determined by this method. However, since the cell was cycled at an ambient temperature of 0 °C with the maximum charging current of 1 C permitted by the cell manufacturer, it is likely that both enhanced SEI building and lithium plating have occurred and formed this layer. Comparing Figs. 8a and 8b to 8c and 8d also exposes a stronger aging behavior in inner areas of the jelly roll as compared to outer areas. We attribute the resulting reinforced delamination of anode and cathode active material in inner areas to the design of the current collector and the stronger windings inside the cell.⁴⁵ Additionally, changes in the DVA can be observed on the cathode side due to a slight shift of NMC_1 toward lower Ah-values. The degradation of the cathode active material can also be detected by the SEM measurement in Fig. 8b, in which burst and broken particles can be detected. However, compared to the fade of the markers on anode side, we interpret the aging mechanisms on anode side as the dominant aging mechanisms for cells aged with the maximum permitted current of 1 C at an ambient temperature of 0 °C.

The parameters of study ② counter these problems by use of a reduced charging current and the omission of the CV discharge sequence. Additionally, the cutoff current during CV charging was increased to 100 mA. Comparing the maximum numbers of EFC between cells of B_2 between studies ① and ②, these changes resulted in relative increases of EFC of 197% , 283%, and 192% for 0 °C, 10 °C, and 25 °C respectively. However, since three parameters were changed between the studies, it is difficult to identify the decisive parameter for the decreased aging rate. Due to the absence of the CV discharge, the expansion of silicon and graphite particles should be reduced, which in turn should reduce particle cracking, loss of contact between particles and current collector, as well as SEI crack and repair processes.^{6,14,4} Since the CC charging current is also reduced, lower potential gradients at surface interfaces should occur, reducing both the polarization behavior and possible lithium-plating phenomena at the end of CC charging.^{6,24}

As shown in Figs. 3a and 3b and Fig. 4a, the parameter adaption contributes to a significant increase in EFC, even if the temperature dependence of the aging behavior remains unchanged. Accordingly, the maximum number of EFC decreases with falling temperatures for both study ① and ②, which is due to the temperature-dependent behavior of the electrode particles, the electrolyte and the kinetics of the reactions in the cell.^{34,46,47} The most significant temperature-dependent parameters affecting the electrode particles and the electrolyte are their conductivities as well as the diffusivity and the molar activity of the electrolyte. The latter is also influenced by the concentration and the transport number of the available lithium ions.^{34,47} Probably the most important parameter for the interaction between the solid and liquid phase is the temperature-dependent exchange current density.^{34,47} At the anode, two competing reactions occur due to the presence of both silicon and graphite particles in the active material of the electrode. During charging at room temperature and at C-rates of 0.1 C or below, the lithiation of silicon is thermodynamically favoured over that of graphite.^{16,48} However, as the temperatures decrease and C-rates increase, seen in this work in particular at rates of 1 C and 0.5 C, the preferred lithiation shifts

toward graphite due to kinetic activation barriers.⁴⁸ This leads to increased concentration and potential gradients between silicon and graphite particles as well as to a higher overpotential between the solid and the liquid phase. The latter in particular also promotes lithium plating.^{47–49,50} As Figs. 3a and 3b and Fig. 4a illustrate, decreasing cycle temperatures lead to noticeable higher aging rates, if equal external load demands are applied. Because the cells were charged and discharged at the same ambient temperature, it is not possible to accurately assess whether charging, discharging, or both caused the increased aging rate at low ambient temperatures, although it is more likely that charging had a greater impact.^{16,48} This suggests that to increase lifetime, preconditioning of the cells should take place when charging at low ambient temperatures using higher C-rates, as expected.

As described, the decreased aging rate can mainly be attributed to improved transport and reaction characteristics at higher temperatures.^{34,46,47} On the other hand, this also promotes side reactions, which in turn would lead to an increased aging rate.^{51,52} Thus, competing processes occur especially for cells cycled at 40 °C in study ①. First, the charging current is set to the maximum charging current of 1 C permitted by the cell manufacturer which in turn provokes increased aging rates, especially lithium plating phenomena at the end of CC charging. Second, the ambient temperature of 40 °C enhances the transport characteristics within the electrolyte and the active material.^{34,46,47} Furthermore, potential gradients at the electrode-electrolyte interface are expected to decrease due to improved reaction kinetics at 40 °C as compared to 25 °C.³⁴ Thus, charge transfer and concentration overpotentials are reduced at 40 °C as compared to 25 °C.³⁴ Consequently, the local anode potential is increased which in turn reduces potential lithium plating phenomena.^{23,42} On the other hand, side reactions are often described to follow an Arrhenius characteristic, which would provoke increased aging rates at an ambient temperature of 40 °C as compared to 25 °C.^{51–57} Therefore, an accurate justification of the aging behavior is difficult due to the competing mechanisms. However, based on the improved aging behavior of the 40 °C cells within study ①, we concluded that it is likely that increased side reactions are dominated by the improved transport and reaction characteristics resulting in a decreased aging rate at the charging current of 1 C for cells aged at an ambient temperature of 40 °C as compared to cells aged at 25 °C. On the other hand, Fig. 4a displays a higher aging rate for cells cycled at 40 °C in study ② as compared to cells cycled at 25 °C. The reasons that this resulted in an increased aging rate in the long term compared to study ① can be explained as follows: Firstly, the charge current was reduced to 0.5 C in study ②, which reduced the risk of lithium plating at the end of CC charging,³⁴ which is why the improved transport and reaction characteristics had a smaller effect on the aging rate. Secondly, cells from study ② totaled almost three times the number of EFC of cells from study ①, which means that the cells were also operated at 40 °C for significantly longer periods of time, allowing more side reactions to occur.

Another noticeable aspect is the variation between the number of EFC at the EOL. During charging and discharging, an inhomogeneous current distribution occurs over both the length (61.5 cm³⁴) and the depth (anode 85 μm , cathode 72.5 μm ¹⁴) of the electrodes.³² The resulting inhomogeneous lithiation or delithiation of the active material leads to locally inhomogeneous stress of electrode particles and therefore to locally inhomogeneous aging intensities.^{14,32,43} In studies ③ to ⑤, one parameter from study ② was changed in each to investigate their influences. In study ③, the CV charging cutoff current was reduced from 100 mA to 33.5 mA to analyze whether this promotes balancing processes within the anode by reducing concentration and polarization gradients and thus diminishing local differences in aging rates. Accordingly, study ③ is expected to mainly affect the aging mechanisms at the anode due to the increased length of CV charging and consequent improvements in the homogeneity of lithiation. On the other hand, the reduced upper voltage limits of studies ④ and ⑤ should predominantly counter

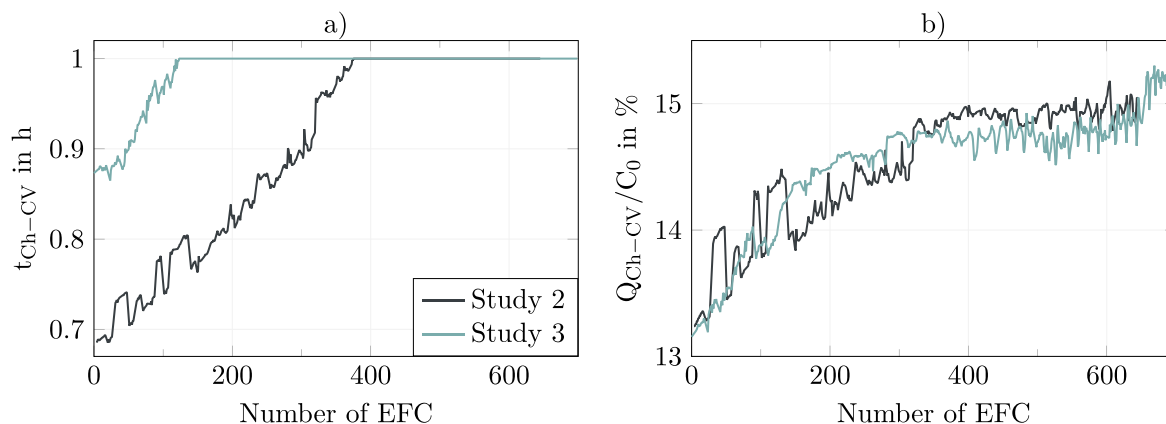


Figure 6. Duration and charge throughput during CV charging within studies ② and ③. No significant differences can be found, since the maximum difference in duration is 0.2 h and the maximum difference in charge throughput is less than 0.8%.

cathode degradation mechanisms by at least partly avoiding voltage ranges known to damage NMC-811.³⁸ The exact voltage level at which NMC-811 becomes unstable for the material combination of SiC/NMC-811 used in this study could not be determined with certainty. Jung et al.³⁸ described voltage values greater than 4.0 V as unstable for the analyzed material combination of C/NMC-811 cells. On the other hand, they formulate more generally that the unstable voltage range coincides with the beginning of the alternative DVA peak. However, since a reduction of the voltage limit to the beginning of the final peak at approximately 4.0 V would have led to a further reduction of usable SOC to 90.3% as compared to 97.36% and 97.98% for 4.089 V and 4.115 V, the voltage limits of studies ④ and ⑤ were chosen, as described above, to obtain a good compromise between voltage reduction and SOC limitation.

In Fig. 5 the results of study ③ can be compared to those of study ②. Extended CV charging in study ③ resulted in an 8% increase in the number of EFC between the cell with the highest number of EFC in study ② and the cell with the highest number of EFC in study ③. Whether or not extended CV charging was also able to reduce the variation between the EFCs at EOL cannot be evaluated as the experiment was terminated before all cells of study ③ reached a SOH level of 80%. However, assuming that the trends seen in the study ③ data at around 645 EFC can be extrapolated to 80% SOH, a smaller final variation is to be expected. The fact that an extended CV charging sequence leads to less intense aging was not expected in view of previous aging studies.^{4,6,14,18–29,31,32}

A decreased CV charging cutoff current causes the cell to be exposed to voltage levels of 4.2 V for longer periods, which encourages side reactions, especially at the NMC-811 cathode.^{14,38} Increased side reactions should in turn give rise to accelerated aging behavior. As shown in Fig. 6a, the durations of the CV charging sequence at the beginning of the experiment differ by about 0.2 h. With increasing numbers of EFC, this temporal difference decreases continuously with some fluctuations until, at around 380 EFC, the CV charge durations reach their maximum permitted values of one hour. In total, the cells in study ③ were held at 4.2 V for around 42 h longer than the cells in study ②, which corresponds to an additional duration of approximately 17%. When comparing the amount of charge throughput during CV charging, a maximum deviation between the studies at equivalent points in their cycles of 0.8% can be seen (see Fig. 6b). This does not appear to be a significant difference. If extended CV charging in study ③ would lead to an increased aging rate of the cathode material, a difference between the cathode markers NMC_I and NMC_{II} of studies ② and ③ could be seen in the DVA of Fig. 7b for the respective cells. However, since the NMC markers are almost superimposed, the DVA proves that no increased aging rate occurred for the cathode active material in study ③ as compared to study ②. Consequently, the influence of additional side reactions of NMC-811 particles during extended CV charging,

which would increase the aging rate, is diminished by another effect of extended CV charging. As described above, Richter et al.⁴⁸ found that for increased C-rates as used within study ③, graphite particles are preferentially lithiated compared to silicon particles, which results in inhomogeneous lithiation between these materials at the end of CC charging. This inhomogeneity is reduced in the subsequent relaxation phase as lithium migrates from graphite to silicon.⁴⁸ These balancing effects cause a more homogeneous lithiation of the silicon and graphite particles within the anode active material, which is induced by the extended length of the CV charging and seems to have a positive influence on the aging rate for the material combination used. The presumed positive influence can in turn be verified with the help of the DVA from Fig. 7b. For studies ② and ③, the main graphite peak C_I as well as the right border are shifted toward lower Ah-values for the aged cells as compared to the DVA of the reference cell at 100% SOH. Additionally, the silicon markers were no longer detectable within the DVA of the aged cells of studies ② and ③. However, the distance between C_I and the right border decreased less in study ③ than in study ②. Furthermore, the main graphite peak C_I is flattened in the DVA of study ②, which indicates inhomogeneous aging of the anode active material.²³ Thus, it can be depicted from DVA that extended CV charging in study ③ led to a decreased and more homogenous aging of the anode active material as compared to study ②. A possible explanation for this would be that due to the more homogeneous lithiation, single particles of graphite and silicon are more uniformly delithiated in the subsequent discharge phase and thus the local aging rate is reduced.

The minimum level of SOH reached in studies ④ and ⑤ amounted to 85% and 82.9% respectively. However, cells in studies ④ and ⑤ have reached even higher numbers of EFC (847/871) as compared to studies ② and ③. A reduction of the voltage window should positively influence the aging rate of both the anode and the cathode. Silicon and graphite particles are lithiated simultaneously for lower C-rates (0.1 C and below).^{16,48} However, at increasing C-rates, the lithiation of silicon slows compared to graphite^{16,48,58} and as studies ④ and ⑤ are subject to C-rates of 0.5 C and diminished upper voltage limits, volumetric expansion of the silicon particles in these studies is expected to be lower than in study ②. Reduced particle swelling should lead to less intense degradation of the anode active material¹⁶ and a higher remaining amount of usable lithium,⁴ thus increasing the remaining capacity and SOH as compared to other studies investigated here. This can be proven by comparing the shifts of the respective anode markers within the DVA shown in Fig. 7c. Due to the increased distance between the main graphite peak C_I and the right border of the DVA of study ④ as compared to study ②, the remaining anode capacity is increased for study ④. On the cathode, reducing the upper voltage limit also reduces particle swelling,^{14,6} but more importantly, it avoids, at least partly, critical phase

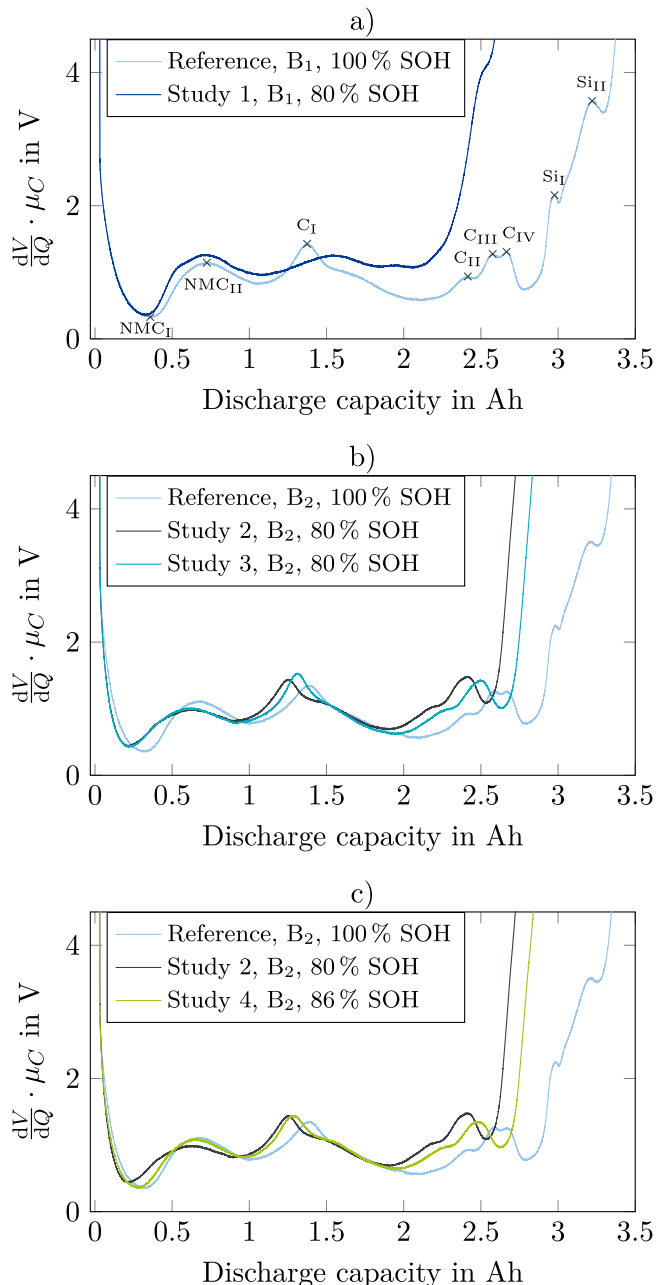


Figure 7. DVA for different temperatures and studies at the end of experiment as compared to the reference DVA at 100% SOH. (a) compares the DVA for a cell of B₁, cycled at an ambient temperature of 0 °C in study ① with the respective reference DVA at 100%. (b) illustrates the effects of an extended CV charging in study ③ as compared to study ② and to the reference. (c) displays the impact of a reduced upper voltage limit in study ④ as compared to study ② and to the reference. The silicon markers S_I and S_{II}, the graphite markers C_I, C_{II}, C_{III}, and C_{IV} as well as the cathode markers NMC_I and NMC_{II} are recorded in (a) as an example for all subfigures.

transitions, as discussed earlier.³⁸ Thus, the aging rate on cathode side is also expected to be decreased in studies ④ and ⑤. The effect of a reduced upper voltage limit on the cathode degradation can therefore be clearly detected by comparing the DVAs of studies ② and ④ with the reference in Fig. 7c. Thus, the cathode marker NMC_I is only slightly shifted toward lower Ah-values for study ④ as compared to the reference DVA, whereas NMC_I is shifted to a greater extend for study ②. Consequently, reducing the upper voltage limit led to a decreased aging rate of the cathode material in study ④. These results are further supported by the microscope and SEM

Table VII. Cell-to-cell variations between the cell with the lowest and highest number of EFC reached, normalized by the mean number of achieved EFC μ of the respective study. All values in %.

Study	Batch	0 °C	10 °C	25 °C	40 °C
①	B ₁	0.00	0.52	0.22	0.13
①	B ₂	0.29	0.15	0.10	—
②	B ₂	0.11	0.07	0.03	0.01
③	B ₂	—	—	0.01	—
④	B ₂	—	—	0.00	—
⑤	B ₂	—	—	0.00	—

measurements, shown in Figs. 8e to 8h. Accordingly, a higher aging rate for inner parts of the jelly roll can also be observed for study ④ for both the anode (e and g) and the cathode (f and h). Compared to the SEM measurement in Fig. 8a, the anode active material particles are only slightly covered with surface layers, which is in good agreement with the DVA results. For the cathode, particle cracking can be partially detected, but the active material seems to be less degraded compared to Fig. 8b.

By comparing the number of EFC reached at SOHs above 80% with the maximum number of EFC at 80% SOH within study ②, the decreased aging rate caused by reduced upper voltage limits becomes also clear, with studies ④ and ⑤ showing increases in EFC of 35% and 31%. As a result, limiting the volumetric expansion of silicon and avoiding critical voltage ranges of the used NMC-811 cathode material by reducing the voltage window can be seen as promising method to extend cell lifetime and decrease variations between individual cells. Additionally, it is worth highlighting that these improvements may be achieved with a loss of less than 3% of the usable SOC range.

Other than the cells of B₂ cycled at an ambient temperature of 25 °C, nonlinear growth of R_i occurs for all cells within study ① (Figs. 3c and 3d). Within study ②, only cells cycled at ambient temperatures of 0 °C and 10 °C show nonlinear growth of R_i (see Fig. 4b). No other studies show nonlinear growth of the R_i (see Fig. 5b). Nonlinear growth is therefore mainly caused by the more demanding charge profile of study ①, temperatures of 10 °C and below (②), or a combination of both. In other words, extended CV charging and reduced upper voltage limits avoided nonlinear growth of R_i . In general, the findings of Keil et al.²⁴ and Schuster et al.,²⁸ which state that capacity fade is in accordance to impedance increase, are confirmed and illustrated in the respective figures. Regarding the estimation of cell EOL, the findings of this present study are that a non-linear increase in R_i is an indicator of a rapidly approaching EOL, whereas the EOL cannot be predicted from a R_i showing a linear increase in resistance.

As Table VI illustrates, cell-to-cell variations vary between 0.0% and 33% in the analyzed studies, with only three cell-to-cell variations of below 7.7%. Based on these variations, the findings of Dubarry et al.³⁹ that low initial cell-to-cell variation would lead to low cell-to-cell variations after cycling cannot be confirmed by the present study. Due to variance in the numbers of EFC completed in each of the studies, only a partial analysis of the values in Table VI is possible. Table VII counters this problem by normalizing the cell-to-cell variations from Table VI with the mean number of EFC achieved in the respective study. The normalized value is assigned to ϵ in the following and is seen as an indicator of cell-to-cell variations, which takes into account the influences of batch, temperature, and cycling profile. Due to a maximum of three cells per study, it must be pointed out here that the calculated values of ϵ are an approximation of the actual cell-to-cell variation, but that there is no absolute statistical certainty. The ability of ϵ to capture the influences of batch, temperature, and cycling profile can be seen in Table VII. Accordingly, ϵ decreases with increasing temperatures within studies ① and ②, which confirms the described temperature dependency. Furthermore, when comparing the variations between B₁ and B₂ within study ①, it can be seen that the values for ϵ are in

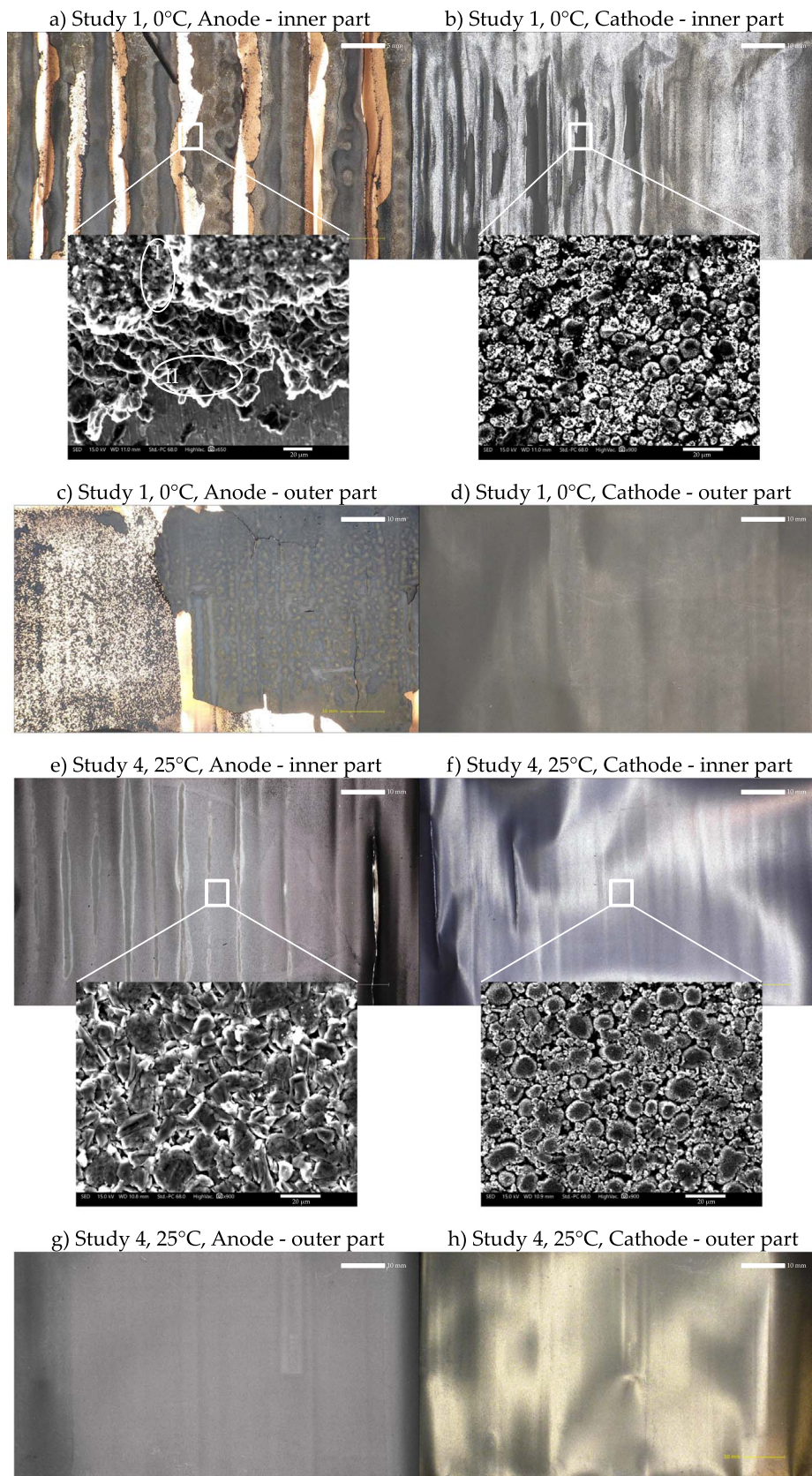


Figure 8. Microscope and SEM analysis for the cell with the highest and lowest aging rate within the experiment. (a) to (d) illustrate microscope analysis of anode and cathode active material from inner and outer parts of the jelly role for the cell with the highest aging rate (study ①, 0 °C). In (a), the circled area I highlights the formed surface layers on the top layer, whereas the circled area II indicates that active material particles in underlying layers are not affected. (e) to (h) show respective analysis for the cell with the lowest aging rate (study ②, reduced upper voltage limit). SEM analysis are shown only for inner parts. The brighter areas in (a), (c), (f), and (h) are due to light reflections during the exposure and have no further significance.

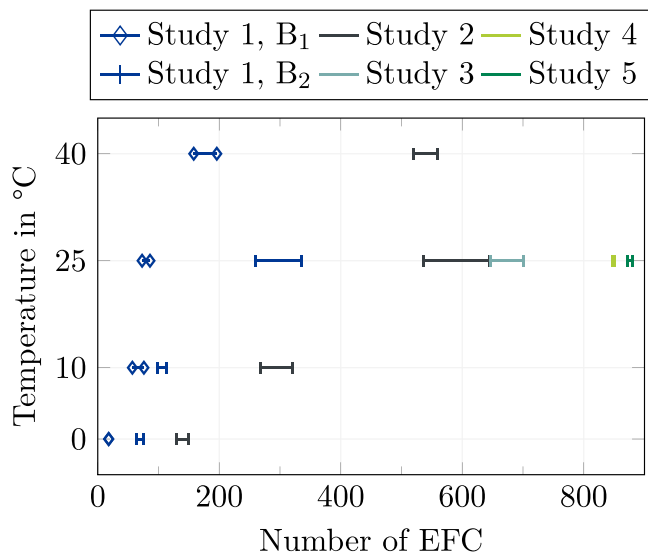


Figure 9. Results of the comprehensive analysis of the aging behavior for LG's MJ1 cells incorporating SiC/NMC-811. The limits of the intervals shown for the different studies and temperatures are defined by the cells with the lowest and highest number of EFC reached. Note that cells of B₁, cycled at an ambient temperature of 0 °C, reached the same number of EFC which is why no interval can be depicted. The figure illustrates the dependency of achievable EFC on the batch, the temperature, and the cycling profile.

general lower for B₂ than for B₁, in particular for corresponding temperatures, which again shows the influence of the reduced silicon content of B₁ vs B₂. For cells from B₁ cycled at 0 °C, the calculated ϵ is an exception, as the aging rate for these cells was so high that no differences in cell-to-cell variations could be seen. The positive influence of extended CV charging and reduced upper voltage limits is also reflected by Table VII. The ϵ of studies ④ and ⑤ in particular underlines the positive effect of avoiding critical voltage levels to decrease cell-to-cell variations over lifetime. Consequently, the statement of Dubarry et al.³⁹ can be extended to the fact that the batch as well as the ambient temperature and the cycling profile have a decisive influence on the long-term development of cell-to-cell variations.

Figure 9 summarizes the results of all presented aging studies and underlines the influence of batch, temperature, and cycling profile on the aging rate of the cells and the variation between the numbers of EFC.

Conclusions

Various studies were performed to investigate the aging behavior of commercial 18650 cells, incorporating SiC anodes and nickel-rich NMC-811 cathodes. Study ① analyzed the influence of varying silicon contents within the anode as well as the temperature dependent aging of two different production batches. The reduced silicon content of B₂ as compared to B₁ was shown to have a major influence on the aging rate of the cells with a greater than fourfold increase in the number of EFC seen at 0 °C. The most likely reason for the improved aging behavior of B₂ is that the reduced silicon content leads to reduced silicon expansion which reduces degradation mechanisms like contact loss or particle and SEI cracking. However, non-linear aging behavior was present for both batches, which, compared to the aging mechanisms described by Li et al.⁶ for the same cell, suggests that an additional aging mechanism caused by lithium plating can be triggered by low temperature operation or increased charging rates, which could be analyzed further by mass spectrometry in future works. The link between decreasing temperatures and decreasing numbers of EFC per cell demonstrated the influence of the ambient temperature during cycling on the SOH progression, regardless of batch and aging profile. This result was expected but it shows yet again the importance of considering preconditioning strategies before charging or discharging cells at low ambient temperatures.

Despite matching the cells by capacity and impedance before the aging experiment, the maximum number of EFC varied by a maximum of 33% at 80% SOH. As such, no correlation between the initial cell-to-cell variation and the aging behavior could be observed, which accords with the findings of Devie et al.⁵⁹ Nonetheless, two strategies were presented to reduce these variations and to increase the cycle life of the analyzed cell. First, longer CV charging seems to promote a more homogeneous lithiation of the particles and demonstrated a positive influence on the lifetime of the cells. Second, avoiding the most damaging voltage areas by reducing the upper voltage limit leads to longer battery life and reduces long-term variations. Including these optimizations in the charging protocols of the cells led to increases in lifetime of up to 35% and reductions in variations between cells of less than 1%. These performance gains were achieved for a loss of less than 3% of the usable SOC. It should be emphasized that through the results of the present work, the findings of Richter et al.⁴⁸ and Jung et al.³⁸ were quantified for the first time by an aging study of commercial cells incorporating SiC/NMC-811. Additionally, the findings of Dubarry et al.³⁹ can be extended by the results of the current study in that low initial cell-to-cell variations are not the only parameter responsible for limited long-term variations, but the ambient temperature and the cycling profile also play a major role in its development.

The relationship between R_i and capacity which has been extensively investigated for established material combinations was confirmed for the investigated cell, despite the incorporation of the relatively novel SiC/NMC-811 material combination. It was shown in particular, that a nonlinear increase in R_i was associated with a nonlinear capacity fade. However, with regard to the estimation of an approaching EOL, the findings of this paper build on those of former authors and show that nonlinear R_i growth can be used as an indicator of an approaching EOL, whereas with a linear increase of R_i , the EOL of the cell has to be detected by capacity loss criteria.

Future studies at the cell level should verify the findings for different cell formats and electrode compositions. Additionally, the influence of the CV discharge sequence by isolated variation of this parameter should be examined in more detail. For interconnected systems and especially for parallel connected cells, additional studies should investigate if longer CV charging and a reduced upper voltage limit have a positive influence on the aging behavior. In particular it would be interesting to study whether these steps can overcome the influence of initial cell-to-cell variations on the aging behavior of cells connected in parallel.

Acknowledgments

The results presented were achieved in association with an INI-TUM project, funded by the AUDI AG. Additionally, this work has received funding from the European Union's Horizon 2020 research and innovation programme under the grant "Electric Vehicle Enhanced Range, Lifetime And Safety Through INGenious battery management" [EVERLASTING-713771].

Appendix

Table A-I. Cell sorting prior to the aging experiment was done to investigate if limited initial cell-to-cell variations result in a low variation of cells' aging behavior.

Cell	Capacity in Ah	R_i in m Ω
Study ① – 0 °C		
cell ₁	3.459	28.3
cell ₂	3.458	28.7
cell ₃	3.458	28.6
Study ① – 10 °C		
cell ₄	3.452	28.8

Table A-I. (Continued).

Cell	Capacity in Ah	R_i in $m\Omega$
cell ₅	3.453	28.6
cell ₆	3.452	29.0
Study ① – 25 °C		
cell ₇	3.452	29.0
cell ₈	3.452	29.0
cell ₉	3.452	29.0
Study ② – 0 °C		
cell ₁₀	3.484	28.6
cell ₁₁	3.484	28.7
cell ₁₂	3.485	28.5
Study ③ – 10 °C		
cell ₁₃	3.483	28.7
cell ₁₄	3.485	28.8
cell ₁₅	3.485	28.8
Study ④ – 25 °C		
cell ₁₆	3.485	28.9
cell ₁₇	3.485	28.9
cell ₁₈	3.485	28.8
Study ⑤ – 40 °C		
cell ₁₉	3.485	28.9
cell ₂₀	3.485	28.9
cell ₂₁	3.484	29.0
Study ⑥ – 25 °C		
cell ₂₂	3.465	28.9
cell ₂₃	3.465	28.8
cell ₂₄	3.465	28.9
Study ⑦ – 25 °C		
cell ₂₅	3.473	28.4
cell ₂₆	3.473	28.5
Study ⑧ – 25 °C		
cell ₂₇	3.473	28.2
cell ₂₈	3.474	28.4

Table A-II. Nomenclature.

Latin symbols		
Symbol	Unit	Description
B		batch
BOL		begin of life
CC		constant current
CV		constant voltage
CC-CV		constant current-constant voltage
DVA		differential voltage analysis
EFC		equivalent full cycles
EIS		electrochemical impedance spectroscopy
EOL		end of life
I	A	applied charge or discharge current
LAM		loss of active material
LIB		lithium-ion battery
LLI		loss of lithium inventory
OCV		open circuit voltage
R_i	Ω	internal impedance
SEI		solid electrolyte interface
SEM		scanning electron microscope

Table A-II. (Continued).

Latin symbols		
SiC		silicon-graphite
SOC		state of charge
SOH		state of health
t_{pause}	h	resting time between charge and discharge
U	V	voltage
Indices		
Symbol		Description
1,2		batch number
Ch		charge
Dch		discharge
max		maximum
min		minimum

ORCID

Markus Schindler  <https://orcid.org/0000-0002-3784-6339>Johannes Sturm  <https://orcid.org/0000-0001-8876-9989>Sebastian Ludwig  <https://orcid.org/0000-0002-6059-9567>Axel Durdel  <https://orcid.org/0000-0002-0479-5491>Andreas Jossen  <https://orcid.org/0000-0003-0964-1405>

References

- G. Zubi, R. Dufo-López, M. Carvalho, and G. Pasaoglu, "The lithium-ion battery: State of the art and future perspectives." *Renew. Sustain. Energy Rev.*, **89**, 292 (2018).
- N. Nitta, P. Oh, W. Wu, J. T. Lee, and G. Yushin, "Li-ion battery materials: present and future." *Mater. Today*, **18**, 252 (2015).
- S. Goriparti, E. Miele, F. de Angelis, E. Di Fabrizio, R. Proietti Zaccaria, and C. Capiglia, "Review on recent progress of nanostructured anode materials for Li-ion batteries." *Journal of Power Sources*, **257**, 421 (2014).
- D. Anseán, G. Baure, M. González, I. Carneán, A. B. García, and M. Dubarry, "Mechanistic investigation of silicon-graphite/LiNi_{0.8}Mn_{0.1}Co_{0.1}O₂ commercial cells for non-intrusive diagnosis and prognosis." *Journal of Power Sources*, **459**, 227882 (2020).
- W. Liu, P. Oh, X. Liu, M.-J. Lee, W. Cho, S. Chae, Y. Kim, and J. Cho, "Nickel-rich layered lithium transition-metal oxide for high-energy lithium-ion batteries." *Angewandte Chemie (International ed. in English)*, **54**, 4440 (2015).
- X. Li, A. M. Colclasure, D. P. Finegan, D. Ren, Y. Shi, X. Feng, L. Cao, Y. Yang, and K. Smith, "Degradation mechanisms of high capacity 18 650 cells containing Si-graphite anode and nickel-rich NMC cathode." *Electrochimica Acta*, **297**, 1109 (2019).
- M. T. McDowell, S. W. Lee, W. D. Nix, and Y. Cui, "XXV anniversary article: Understanding the lithiation of silicon and other alloying anodes for lithium-ion batteries." *Advanced materials (Deerfield Beach, Fla.)*, **25**, 4966 (2013).
- F. Jeschull, Y. Surace, S. Zürcher, G. Lari, M. E. Spahr, P. Novák, and S. Tragesinger, "Graphite Particle-Size Induced Morphological and Performance Changes of Graphite-Silicon Electrodes." *J. Electrochem. Soc.*, **167**, 100535 (2020).
- C. He, S. Wu, N. Zhao, C. Shi, E. Liu, and J. Li, "Carbon-encapsulated Fe₃O₄ nanoparticles as a high-rate lithium ion battery anode material." *ACS Nano*, **7**, 4459 (2013).
- G. Zhang, L. Yu, H. B. Wu, H. E. Hoster, and X. W. D. Lou, "Formation of ZnMn₂O₄ ball-in-ball hollow microspheres as a high-performance anode for lithium-ion batteries." *Advanced materials (Deerfield Beach, Fla.)*, **24**, 4609 (2012).
- X. Wang, L. Qiao, X. Sun, X. Li, D. Hu, Q. Zhang, and D. He, "Mesoporous NiO nanosheet networks as high performance anodes for Li ion batteries." *Journal of Materials Chemistry A*, **1**, 4173 (2013).
- J. Yang, "Sub-Microcrystalline Sn and Sn-SnSb Powders as Lithium Storage Materials for Lithium-Ion Batteries." *Electrochem. Solid-State Lett.*, **2**, 161 (1999).
- S. Bourderau, T. Brousse, and D. Schleich, "Amorphous silicon as a possible anode material for Li-ion batteries." *Journal of Power Sources*, **81-82**, 233 (1999).
- T. M. M. Heenan, A. Jnawali, M. D. R. Kok, T. G. Tranter, C. Tan, A. Dimitrijevic, R. Jervis, D. J. L. Brett, and P. R. Shearing, "An Advanced Microstructural and Electrochemical Datasheet on 18 650 Li-Ion Batteries with Nickel-Rich NMC811 Cathodes and Graphite-Silicon Anodes." *J. Electrochem. Soc.*, **167**, 140530 (2020).
- Y. Reynier, C. Vincens, C. Leys, B. Amestoy, E. Mayousse, B. Chavillon, L. Blanc, E. Gutel, W. Porcher, T. Hirose, and C. Matsui, "Practical implementation of Li doped SiO in high energy density 21 700 cell." *Journal of Power Sources*, **450**, 227699 (2020).
- P.-F. Lory, B. Mathieu, S. Genies, Y. Reynier, A. Boulineau, W. Hong, and M. Chandresis, "Probing Silicon Lithiation in Silicon-Carbon Blended Anodes with a Multi-Scale Porous Electrode Model." *J. Electrochem. Soc.*, **167**, 120506 (2020).
- F. Ozanam and M. Rosso, "Silicon as anode material for Li-ion batteries." *Materials Science and Engineering: B*, **213**, 2 (2016).
- T. Baumhöfer, M. Brühl, S. Rothgang, and D. U. Sauer, "Production caused variation in capacity aging trend and correlation to initial cell performance." *Journal of Power Sources*, **247**, 332 (2014).

19. M. Bercibar, M. Dubarry, I. Villarreal, N. Omar, and J. van Mierlo, *Degradation Mechanisms Detection for HP and HE NMC Cells Based on Incremental Capacity Curves*, in: *2016 IEEE Vehicle Power and Propulsion Conference (VPPC)* (IEEE, Piscataway, NJ) 1 (2016).
20. M. Dubarry, N. Qin, and P. Brooker, "Calendar aging of commercial Li-ion cells of different chemistries—A review." *Current Opinion in Electrochemistry*, **9**, 106 (2018).
21. M. Ecker, N. Nieto, S. Käbitz, J. Schmalstieg, H. Blanke, A. Warnecke, and D. U. Sauer, "Calendar and cycle life study of Li(NiMnCo)O₂-based 18 650 lithium-ion batteries." *Journal of Power Sources*, **248**, 839 (2014).
22. A. S. Keefe, R. Weber, I. G. Hill, and J. R. Dahn, "Studies of the SEI layers in Li(Ni 0.5Mn0.3Co 0.2)O₂/Artificial Graphite Cells after Formation and after Cycling." *J. Electrochem. Soc.*, **167**, 120507 (2020).
23. P. Keil and A. Jossen, "Calendar Aging of NCA Lithium-Ion Batteries Investigated by Differential Voltage Analysis and Coulomb Tracking." *J. Electrochem. Soc.*, **164**, A6066 (2017).
24. J. Keil, N. Paul, V. Baran, P. Keil, R. Gilles, and A. Jossen, "Linear and Nonlinear Aging of Lithium-Ion Cells Investigated by Electrochemical Analysis and In-Situ Neutron Diffraction." *J. Electrochem. Soc.*, **166**, A3908 (2019).
25. C.-H. Lee, Z.-Y. Wu, S.-H. Hsu, and J.-A. Jiang, "Cycle Life Study of Li-Ion Batteries With an Aging-Level-Based Charging Method." *IEEE Transactions on Energy Conversion*, **35**, 1475 (2020).
26. M. Lewerenz, G. Fuchs, L. Becker, and D. U. Sauer, "Irreversible calendar aging and quantification of the reversible capacity loss caused by anode overhang." *Journal of Energy Storage*, **18**, 149 (2018).
27. M. Naumann, F. B. Spingler, and A. Jossen, "Analysis and modeling of cycle aging of a commercial LiFePO₄/graphite cell." *Journal of Power Sources*, **451**, 227666 (2020).
28. S. F. Schuster, M. J. Brand, C. Campestrini, M. Gleissenberger, and A. Jossen, "Correlation between capacity and impedance of lithium-ion cells during calendar and cycle life." *Journal of Power Sources*, **305**, 191 (2016).
29. A. Yang, Y. Wang, F. Yang, D. Wang, Y. Zi, K. L. Tsui, and B. Zhang, "A comprehensive investigation of lithium-ion battery degradation performance at different discharge rates." *Journal of Power Sources*, **443**, 227108 (2019).
30. X. Han, L. Lu, Y. Zheng, X. Feng, Z. Li, J. Li, and M. Ouyang, "A review on the key issues of the lithium ion battery degradation among the whole life cycle." *eTransportation*, **1**, 100005 (2019).
31. H. Popp, N. Zhang, M. Jahn, M. Arrinda, S. Ritz, M. Faber, D. U. Sauer, P. Azais, and I. Cendoya, "Ante-mortem analysis, electrical, thermal, and ageing testing of state-of-the-art cylindrical lithium-ion cells." *e & i Elektrotechnik und Informationstechnik*, **137**, 169 (2020).
32. M. D. R. Kok, J. B. Robinson, J. S. Weaving, A. Jnawali, M. Pham, F. Iacoviello, D. J. L. Brett, and P. R. Shearing, "Virtual unrolling of spirally-wound lithium-ion cells for correlative degradation studies and predictive fault detection." *Sustainable Energy & Fuels*, **3**, 2972 (2019).
33. I. Zilberman, S. Ludwig, and A. Jossen, "Cell-to-cell variation of calendar aging and reversible self-discharge in 18 650 nickel-rich, silicon-graphite lithium-ion cells." *Journal of Energy Storage*, **26**, 100900 (2019).
34. J. Sturm, A. Rheinfeld, I. Zilberman, F. B. Spingler, S. Kosch, F. Frie, and A. Jossen, "Modeling and simulation of inhomogeneities in a 18 650 nickel-rich, silicon-graphite lithium-ion cell during fast charging." *Journal of Power Sources*, **412**, 204 (2019).
35. M. Schindler, A. Durdul, J. Sturm, P. Jocher, and A. Jossen, "On the Impact of Internal Cross-Linking and Connection Properties on the Current Distribution in Lithium-Ion Battery Modules." *J. Electrochem. Soc.*, **167**, 120542 (2020).
36. M. Schindler, J. Sturm, S. Ludwig, J. Schmitt, and A. Jossen, "Evolution of Initial Cell-to-Cell Variations During a Three-Year Production Cycle." *eTransportation*, **8**, 100102 (2021).
37. M. Pharr, K. Zhao, X. Wang, Z. Suo, and J. J. Vlassak, "Kinetics of initial lithiation of crystalline silicon electrodes of lithium-ion batteries." *Nano Lett.*, **12**, 5039 (2012).
38. R. Jung, M. Metzger, F. Maglia, C. Stinner, and H. A. Gasteiger, "Oxygen Release and Its Effect on the Cycling Stability of LiNi_xMn_yCo_zO₂(NMC) Cathode Materials for Li-Ion Batteries." *J. Electrochem. Soc.*, **164**, A1361 (2017).
39. M. Dubarry, C. Truchot, M. Cugnet, B. Y. Liaw, K. Gering, S. Sazhin, D. Jamison, and C. Michelbacher, "Evaluation of commercial lithium-ion cells based on composite positive electrode for plug-in hybrid electric vehicle applications. Part I: Initial characterizations." *Journal of Power Sources*, **196**, 10328 (2011).
40. I. Cendoya, "Selection of commercial cells to fit a multiple purpose modular battery pack concept: iModBatt." *International EV Batteries 2018: Cost-Effective Engineering for Hybrid and Electric Vehicles*, Twickenham Stadium, London (2018).
41. F. M. Kindermann, A. Noel, S. V. Erhard, and A. Jossen, "Long-term equalization effects in Li-ion batteries due to local state of charge inhomogeneities and their impact on impedance measurements." *Electrochimica Acta*, **185**, 107 (2015).
42. I. Zilberman, S. Ludwig, M. Schiller, and A. Jossen, "Online aging determination in lithium-ion battery module with forced temperature gradient." *Journal of Energy Storage*, **28**, 101170 (2020).
43. F. M. Kindermann, P. J. Osswald, G. Ehler, J. Schuster, A. Rheinfeld, and A. Jossen, "Reducing Inhomogeneous Current Density Distribution in Graphite Electrodes by Design Variation." *J. Electrochem. Soc.*, **164**, E3105 (2017).
44. P. Keil, *Aging of Lithium-Ion Batteries in Electric Vehicles*, Technische Universität München (2017).
45. J. Sturm, A. Frank, A. Rheinfeld, S. V. Erhard, and A. Jossen, "Impact of Electrode and Cell Design on Fast Charging Capabilities of Cylindrical Lithium-Ion Batteries." *J. Electrochem. Soc.*, **167**, 130505 (2020).
46. A. Jossen, "Fundamentals of battery dynamics." *Journal of Power Sources*, **154**, 530 (2006).
47. J. Schmalstieg, *Physikalisch-elektrochemische Simulation von Lithium-Ionen-Batterien: Implementierung, Parametrierung und Anwendung*, Aachener Beiträge des ISEA, RWTH Aachen (2017), <http://publications.rwth-aachen.de/record/689927/files/689927.pdf>.
48. K. Richter, T. Waldmann, N. Paul, N. Jobst, R.-G. Scurtu, M. Hofmann, R. Gilles, and M. Wohlfahrt-Mehrens, "Low-Temperature Charging and Aging Mechanisms of Si/C Composite Anodes in Li-Ion Batteries: An Operando Neutron Scattering Study." *ChemSusChem*, **13**, 529 (2020).
49. A. Rheinfeld, J. Sturm, A. Noel, J. Wilhelm, A. Kriston, A. Pfrang, and A. Jossen, "Quasi-Isothermal External Short Circuit Tests Applied to Lithium-Ion Cells: Part II. Modeling and Simulation." *J. Electrochem. Soc.*, **166**, A151 (2019).
50. A. Nyman, T. G. Zavalis, R. Elger, M. Behm, and G. Lindbergh (ed.), *A New Methodology for Evaluating the High-Power Behavior of a Li-Ion Battery Cell*, ECS Transactions (The Electrochemical Society, Vienna, Austria) (2010).
51. T. Waldmann, B.-I. Hogg, and M. Wohlfahrt-Mehrens, "Li plating as unwanted side reaction in commercial Li-ion cells—A review." *Journal of Power Sources*, **384**, 107 (2018).
52. I. Zilberman, J. Sturm, and A. Jossen, "Reversible self-discharge and calendar aging of 18 650 nickel-rich, silicon-graphite lithium-ion cells." *Journal of Power Sources*, **425**, 217 (2019).
53. S. Arrhenius, "About the inversion rate of sucrose caused by acids." *Z. Phys. Chem.*, **4U**, 1 (1889).
54. M. P. Klein and J. W. Park, "Effects of Non-Uniform Temperature on In-Situ Current Distribution and Non-Uniform State of Charge Measurements for LiFePO₄ and LiNiMnCoO₂ Cells." *ECS Trans.*, **77**, 81 (2017).
55. J. Mao, W. Tiedemann, and J. Newman, "Simulation of temperature rise in Li-ion cells at very high currents." *Journal of Power Sources*, **271**, 444 (2014).
56. Y. Troxler, B. Wu, M. Marinescu, V. Yufit, Y. Patel, A. J. Marquis, N. P. Brandon, and G. J. Offer, "The effect of thermal gradients on the performance of lithium-ion batteries." *Journal of Power Sources*, **247**, 1018 (2014).
57. N. Yang, X. Zhang, B. Shang, and G. Li, "Unbalanced discharging and aging due to temperature differences among the cells in a lithium-ion battery pack with parallel combination." *Journal of Power Sources*, **306**, 733 (2016).
58. M. Wetjen, S. Solchenbach, D. Pritzl, J. Hou, V. Tileli, and H. A. Gasteiger, "Morphological Changes of Silicon Nanoparticles and the Influence of Cutoff Potentials in Silicon-Graphite Electrodes." *J. Electrochem. Soc.*, **165**, A1503 (2018).
59. A. Devie, G. Baure, and M. Dubarry, "Intrinsic Variability in the Degradation of a Batch of Commercial 18 650 Lithium-Ion Cells." *Energies*, **11**, 1031 (2018).